Research Article

Effects of Unbalanced Lamination Parameters on the Static Aeroelasticity of a High Aspect Ratio Wing

JinYang Li [iD]**, JunLi Wang** [iD]**, ZhiGui Ren, and WeiFeng Wei**

Mechanical Engineering College, Shaanxi University of Technology, Hanzhong 723000, China

Correspondence should be addressed to JunLi Wang; wjl503@126.com

In this paper, in order to understand the influence of the unbalanced coefficient of composite laminates on the static aeroelasticity of high aspect wings, a series of numerical simulation calculations were carried out, and this work wants to provide some reference for the structural design of aircraft. Considering the influence of geometric nonlinearity, the unidirectional fluid-solid coupling calculation method based on loose coupling is used to control the change of unbalanced coefficient of laminates on the basis of layering angle, layering thickness, and layering region, so as to observe the changes caused to the wings. The relationship between the unbalanced coefficient and the constant thickness layup and the variable thickness layup with $0°$ and $±45°$ layup angles was studied, respectively. Then, the layup angle of $90°$ was added to study the influence of the unbalanced coefficient on the static aeroelasticity of the wing structure with the change of the layup angle and the different choice of layup region. The results show that the deformation is the smallest when the unbalanced coefficient is 0.5, and the deformation trend is evenly distributed along both sides when the unbalanced coefficient is 0.5. When the unbalanced coefficient is changed, adding the $90°$ layup angle can significantly reduce the overall deformation of the wing and show different sensitivity characteristics to different layup areas. The increase of the unbalanced coefficient makes the chordal displacement gradually change from linear distribution to nonlinear distribution along the spread direction, and the displacement will gradually decrease.

1. Introduction

Advanced composite material (ACM) was born in the late 1960s. In the early 1970s, the U.S. Air Force Materials Research Institute applied composite materials to the structure of fighter aircraft in order to improve the performance of military fighter aircraft. Since 1980, the US Navy has applied a large number of advanced composite materials to the latest fighter aircraft, starting with the F/A-18 carrier-based multirole fighter aircraft. For example, the composite material on the USAF's F-22 "Raptor" fighter aircraft occupies 25% of the weight of the structure, the composite material on the B-2 "Ghost" bomber aircraft occupies 50% of the weight of the structure, and the composite material consumption of the "Predator" UAV even reaches 92% of the total weight of the structure [1, 2]. Similarly, in the civil aviation market, B787 and A380 of the world's top two airlines, led by Boeing and Airbus, use composite materials for 50% and 52%, respectively [3, 4]. Composite materials have gradually replaced metal and alloy to some extent and become the "new favorite" in aviation design and manufacturing. It can be said that the application of composite material science and technology has promoted the rapid development of modern aircraft structural design. Compared with the traditional metal materials, the composite material has the characteristics of high specific strength, high specific stiffness, strong fatigue corrosion resistance, and low thermal expansion coefficient, so it is easier to design the body structure with light weight, large bearing force, and small deformation. In modern aircraft design with high aspect ratio, aeroelastic design of composite wing is of great significance due to the characteristics of large wing flexibility and small stiffness [5]. In order to optimize the flight performance and aeroelastic characteristics of aircraft with high aspect

ratio, aeroelastic tailoring technology is often needed, and the comprehensive design of layering number, angle, and sequence is usually carried out.

With the increasing maturity of composite material technology and aerodynamic tailoring technology, coupled with its extensive application in aircraft design engineering practice, more and more researchers are devoted to the research of composite material aircraft layup and structure. In the aspect of aeroelastic tailoring design, the main work at present is to study the structural parameters such as laminate order, laminate thickness, and laminate proportion of composite materials and explore the influence of parameter allocation on aeroelastic characteristics of the wings. Wan et al. [6] studied the aeroelastic effects of unevenly laid wings with high aspect ratio by unevenly laid wings. Liang et al. [7] carried out aeroelastic optimization design for composite wing panels of large aircraft and obtained reasonable distribution of lamination proportion. Zhou et al. [8] studied the influence of composite lamination parameters on aeroelasticity optimization of the wing with high aspect ratio, and the results showed that the skin-unbalanced lamination mainly affected the aeroelasticity of the wing. Xu et al. [9] changed the symmetry and equilibrium of the laminated plate by adding the laminated layer on top of the symmetrical laminated layer and obtained the ideal position of the added layer and laying angle. Xingyin et al. and Zhang et al. [10, 11] focused on the coupling analysis of bending and torsion deformation of asymmetric/unbalanced laminates by using experimental methods. Wang et al. [12] explored and optimized the layup angle so as to reduce the deformation of the wing with high aspect ratio and effectively improve the aeroelastic characteristics of the wing. Basri et al. [13] studied layup combination structures with different angles and further determined the optimal layup combination for the leading edge of the wing with nodules. Koohi et al. and Xie et al. [14, 15] carried out aeroelastic analysis on the composite wing beam model with high aspect ratio on the basis of considering geometric large deformation and achieved a good calculation accuracy. Kirsch et al. [16] developed the GEBTAero code to evaluate the aeroelastic tailoring effect and carry out numerical calculation. Bourchak and Dobah [17] designed a modified wing with good performance by simulation and experiment on the deformed wing from the perspective of layup, nonequilibrium, layup number, and layup position. Dillinger et al. [18] proposed a modified model for static aeroelastic aerodynamic load of composite wing and successfully applied it to stiffness optimization of forward swept wing. Bramsiepe et al. and Yu et al. [19, 20] carried out numerical simulation of maneuver load and gust load of composite flying wing UAV and carried out parameter optimization design. Shrivastava et al. [21] adopted the combination of classical genetic algorithm and CAE to carry out weight optimization design for a transport aircraft wing and achieved the expected calculation results. DLR-AE [22] at the Aero-Elastic Research Institute of the German Aerospace Center calculated the aeroelastic response of the composite wing under multiple working conditions using internal development tools and compared it with that of the aluminum alloy structure wing.

Some other researches mainly focus on the mathematical model construction of laminates; the purpose of which is to describe the mechanical properties of laminates more accurately and provide some theoretical basis for engineering design. Shukla and Singh [23] used the radial basis function to analyze the flexure of the laminates and derived the governing differential equation using the energy principle. Then, the accuracy of the method was verified by using MATLAB software to write a program. Kwon [24] studied the failure of composite structures under hydrodynamic loads by means of fluid-solid coupling numerical simulation and then discussed the multiscale modeling method of composite laminates. Guillén-Rujano et al. [25] derived a new calculation formula for composite laminates by using the first-order shear deformation theory and the minimum potential energy theorem. This formula can be used to calculate the bending and torsion problems of composite laminates well, and the calculation accuracy is in good agreement with the experimental data. Thakur et al. [26] proposed a finite element model of C^0 laminated plates, which used von Karman and green-Lagrangian strain-displacement relation to simulate geometric nonlinearity and then derived the nonlinear motion governing equation by using Hamiltonian principle. Finally, the Newton-Raphson method was used to solve the problem. The calculated results are reliable and efficient, which can solve the free vibration and forced vibration of composite laminates. Yang and Yang [27] analyzed the dynamics of laminated plates under nonlinear elastic constraints, established different binding models, and obtained the transverse displacement of laminated plates through transient analysis. Using the analysis principle of micromechanics, Nallim et al. [28] proposed a variational formula for the analysis of the free vibration of the elastic constraint asymmetric composite laminates and gave the influence of different mechanical and geometric parameters on the dynamic properties of different laminates. Hafizah et al. [29] studied the free vibration problem of laminated plates with antisymmetric angles of varying thickness. By introducing the theory of high-order shear deformation plates, the shear correction factor was successfully eliminated and the accuracy of transverse shear stress was improved. Liu et al.'s [30] laminated plate is studied in the nonlinear response of a subsonic condition, using the Hamilton's principle, the composite laminated plate is established in subsonic aerodynamic force motion control of nonlinear partial differential equation, and the frequency response curve under different parameters is obtained; thus, the exciting force and laminated plate structure provide reference for the coupling problem.

In summary, the above studies are mainly divided into two aspects. On the one hand, the performance design of structural parameters such as laying angle, laying order, and asymmetry/unbalanced of high aspect ratio composite wing was carried out, or the sensitivity algorithm and genetic algorithm were used to optimize the aeroelasticity of composite wing. On the other hand, a more accurate and efficient calculation method is obtained by studying the mathematical model of laminates and deriving their constitutive equations. However, in the current design of composite materials for aircraft, few studies have paid attention to the changes in the mechanical properties of laminates caused
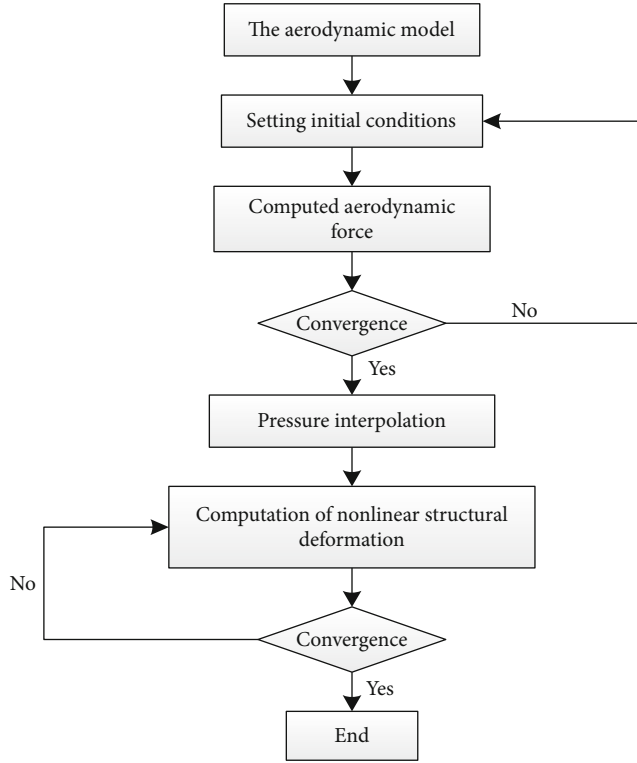
FIGURE 1: Calculation process.

by the changes in unbalanced coefficients, and few studies have involved the effects of the differences in unbalanced coefficients on the static aeroelasticity of aircraft with high aspect ratio. The theoretical system of composite wing structure design still has some shortcomings. Therefore, based on the calculation method of fluid-structure interaction, this paper focuses on the analysis of the static aeroelasticity of high aspect ratio wing under different unbalanced coefficients (layer disequalization coefficient, i.e., the ratio of the number of layers on the upper/lower 45° wing surface to the number of layers on the upper/lower 45° wing surface and the number of layers on the upper/lower 45° wing surface and -45° wing surface), the layer thickness, angle, and the influence of each layer segment on the static aeroelasticity.

In the first part, the theoretical solution method of static aeroelasticity is introduced. In the second part, the establishment of the finite element model of the wing with high aspect ratio and the design of the layup thickness, angle, and wing segment are described in detail. In the third part, the effects of various variables on the aerostatic elasticity of the wings with high aspect ratio are analyzed under different unbalanced coefficients.

2. Computational Theory

2.1. Calculation Method.
Compared with the vortex lattice method in the common static aeroelastic analysis, the unidirectional fluid-solid coupling method based on loose coupling has the advantages of fast calculation speed and relatively high accuracy. In the numerical simulation, the

Navier-Stokes equation is used as the governing equation to solve the aerodynamic load by the finite volume method. If the aerodynamic load converges, the interpolation method is used to insert it into the structural grid nodes. Finally, the finite element method and Newton-Raphson iterative method are used to solve the structural equation under aerodynamic force, and the deformation and stress-strain values of the wing structure with high aspect ratio are obtained. The specific implementation process is shown in Figure 1.

2.2. Aerodynamic Calculation.
Using the Euler description method, the differential form of three-dimensional conservation N-S equation in Cartesian coordinate system is as follows [30–33]:

$$\frac{\partial \mathbf{W}}{\partial t} + \frac{\partial \mathbf{f}}{\partial x} + \frac{\partial \mathbf{g}}{\partial y} + \frac{\partial \mathbf{q}}{\partial z} = \frac{\partial \mathbf{R}}{\partial x} + \frac{\partial \mathbf{S}}{\partial y} + \frac{\partial \mathbf{T}}{\partial z}, \tag{1}$$

where W is the conserved variable vector, i.e.,

$$W = \begin{bmatrix} \rho \\ \rho_u \\ \rho_v \\ \rho_w \\ \rho_E \end{bmatrix}. \tag{2}$$

f, g, and q are the convective flux vectors, i.e.,

$$f = \begin{bmatrix} \rho u \\ \rho u^2 + p \\ \rho uv \\ \rho uw \\ \rho uE + up \end{bmatrix},$$

$$g = \begin{bmatrix} \rho v \\ \rho vu \\ \rho v^2 + p \\ \rho vw \\ \rho vE + vp \end{bmatrix}, \tag{3}$$

$$q = \begin{bmatrix} \rho w \\ \rho wu \\ \rho wv \\ \rho w^2 + p \\ \rho wE + wp \end{bmatrix}.$$

R, S, and T are viscous flux vectors, i.e.,

$$R = \begin{bmatrix} 0 \\ \tau_{xx} \\ \tau_{yx} \\ \tau_{zx} \\ \varphi_x \end{bmatrix},$$

$$S = \begin{bmatrix} 0 \\ \tau_{xy} \\ \tau_{yy} \\ \tau_{zy} \\ \varphi_y \end{bmatrix}, \tag{4}$$

$$T = \begin{bmatrix} 0 \\ \tau_{xz} \\ \tau_{yz} \\ \tau_{zz} \\ \varphi_z \end{bmatrix}.$$

Among them,

$$\begin{cases} \varphi_x = u\tau_{xx} + v\tau_{xy} + w\tau_{xz} + k\dfrac{\partial T}{\partial x}, \\ \varphi_y = u\tau_{yx} + v\tau_{yy} + w\tau_{yz} + k\dfrac{\partial T}{\partial y}, \\ \varphi_z = u\tau_{zx} + v\tau_{zy} + w\tau_{zz} + k\dfrac{\partial T}{\partial z}. \end{cases} \tag{5}$$

For Newtonian fluid, the formula for calculating the viscous stress τ_{ij} is as follows:

$$\begin{cases} \tau_{xx} = 2\mu u_x - \dfrac{2}{3}\mu(u_x + v_y + w_z), \tau_{xy} = \tau_{yx} = \mu(u_y + v_x), \\ \tau_{yy} = 2\mu v_y - \dfrac{2}{3}\mu(u_x + v_y + w_z), \tau_{xz} = \tau_{zx} = \mu(u_z + w_x), \\ \tau_{zz} = 2\mu w_z - \dfrac{2}{3}\mu(u_x + v_y + w_z), \tau_{yz} = \tau_{zy} = \mu(v_z + w_y). \end{cases} \tag{6}$$

In order to make the N-S equation closed, the state equation is introduced as follows:

$$p = (\gamma - 1)\rho\left[E - \frac{1}{2}(u^2 + v^2 + w^2)\right], \tag{7}$$

where p is the fluid pressure, ρ is the fluid density, E is the total fluid energy per unit mass, u, v, and w are the three velocity components of fluid velocity V in the Cartesian coordinate system, τ_{ij} is the component of the viscous stress

term $\bar{\bar{\tau}}$, γ is the specific heat ratio, T is the fluid temperature, k is the fluid conductivity coefficient, and μ is the viscosity coefficient of the fluid.

The viscosity coefficient of air is generally calculated according to Sutherland formula, and its expression is as follows:

$$\frac{\mu}{\mu_0} = \frac{T_0 + C}{T + C}\left(\frac{T}{T_0}\right)^{1.5}. \tag{8}$$

In the equation, T_0 and μ_0 are the temperature and viscosity coefficient of the standard atmosphere at sea level, respectively. $T_0 = 288.15$ K and $\mu_0 = 1.7894 \times 10^{-5}$ N $\cdot$ s/m^2. The constant $C = 110.4k$.

The relationship between the heat conduction coefficient and viscosity coefficient of a complete gas is as follows:

$$k = c_p\frac{\mu}{P_r}, \tag{9}$$

where c_p is the isobaric specific heat capacity, P_r is Prandtl number, and P_r of laminar air is 0.72.

2.3. Structural Calculation. In structural calculation, its equilibrium equation can be expressed as follows [33–37]:

$$\mathbf{M\ddot{u}} + \mathbf{C\dot{u}} + \mathbf{Ku} = \mathbf{F}. \tag{10}$$

When the geometrically nonlinear problem of large deformation is involved, the stiffness matrix $\mathbf{K}$ can be expressed as follows [38]:

$$\mathbf{K} = \mathbf{K^{inc}} + \mathbf{K^u} - \mathbf{K^a}, \tag{11}$$

where $\mathbf{M}$ is the mass matrix, $\mathbf{C}$ is the damping matrix, $\mathbf{K}$ is the stiffness matrix, $\mathbf{u}$ is the displacement vector, $\mathbf{u}$ is the velocity vector, $\mathbf{\ddot{u}}$ is the acceleration vector, $\{F(t)\}$ is the force vector, $\mathbf{K^{inc}}$ is the main tangential stiffness matrix, $\mathbf{K^u}$ is the large displacement stiffness matrix, and $\mathbf{K^a}$ is the initial load matrix.

2.4. Coupled Data Transfer. In order to improve the computational accuracy of geometrical nonlinearity of structures, the interpolation accuracy of fluid-structure interface will play an important role in the calculation. The conserved interpolation method is used to satisfy the data exchange of the coupling surface. In the case of upper-solid coupling of coupling interface, it can be expressed as follows [39]:

$$\begin{aligned} u_f &= \mathbf{H}u_s, \\ \delta u_f \cdot f_a &= \delta u_s{}^T \cdot f_s, \end{aligned} \tag{12}$$

where u_f is the pneumatic point displacement, u_s is the structural point displacement, $\mathbf{H}$ is the interpolation matrix, f_a is the aerodynamic load, f_s is the equivalent load of structure, and δu_f and δu_s are the virtual displacements of aerodynamic points and structural points, respectively.

If **H** is independent of displacement, then

$$\delta u_f = \mathbf{H} \cdot \delta u_s. \tag{13}$$

Then, the relationship between equivalent load of structure and aerodynamic load is obtained, i.e.,

$$f_s = \mathbf{H}^T \cdot f_a. \tag{14}$$

The coupling diagram is shown in Figure 2.

2.5. Laminate Calculation. The classical laminate theory has the following assumptions: (1) the bond layer between the laminates is very thin and firmly bonded, and no slip occurs between the laminates. (2) The laminates are thin plates, the thickness of the laminates is constant, and the single-layer laminates are analyzed according to the plane stress state. (3) The bending deformation of the laminate is in the range of small deflection. Before deformation, it is perpendicular to the straight line of the middle plane. After deformation, it remains straight and perpendicular to the middle plane, and the length of the straight line remains unchanged.

Suppose that the displacement of any point C in the distance plane z along the three coordinate axes x, y, and z direction is $u(x, y, z)$, $v(x, y, z)$, and $w(x, y, z)$, respectively, then the classical laminate theory can be obtained [39]:

$$\begin{cases} u(x, y, z) = u_0(x, y) - z \dfrac{\partial w(x, y)}{\partial x}, \\ v(x, y, z) = v_0(x, y) - z \dfrac{\partial w(x, y)}{\partial y}, \\ w(x, y) = w_0(x, y), \end{cases} \tag{15}$$

where $u_0(x, y)$, $v_0(x, y)$, and $w_0(x, y)$ are the displacements of the middle plane of the laminates.

Then, the strain-displacement geometric relationship is as follows:

$$\begin{cases} \varepsilon_x = \dfrac{\partial u}{\partial x}, \gamma_{yz} = \dfrac{\partial w}{\partial y} + \dfrac{\partial z}{\partial x}, \\ \varepsilon_y = \dfrac{\partial v}{\partial y}, \gamma_{zx} = \dfrac{\partial w}{\partial x} + \dfrac{\partial u}{\partial z}, \\ \varepsilon_z = \dfrac{\partial w}{\partial z}, \gamma_{xy} = \dfrac{\partial u}{\partial y} + \dfrac{\partial v}{\partial x}. \end{cases} \tag{16}$$

It is calculated as follows:

$$\begin{cases} \varepsilon_x = \dfrac{\partial u_0}{\partial x} - z \dfrac{\partial^2 w}{\partial x^2} = \varepsilon_x^{\,0} + z k_x, \\ \varepsilon_y = \dfrac{\partial v_0}{\partial y} - z \dfrac{\partial^2 w}{\partial y^2} = \varepsilon_y^{\,0} + z k_y, \\ \gamma_{xy} = \dfrac{\partial u_0}{\partial x} + \dfrac{\partial v_0}{\partial y} - 2z \dfrac{\partial^2 w}{\partial x \partial y} = \gamma_{xy}^{\,0} + z k_{xy}, \end{cases} \tag{17}$$

where $\varepsilon_x^{\,0}$, $\varepsilon_y^{\,0}$, and $\gamma_{xy}^{\,0}$ are the strains in the middle of the
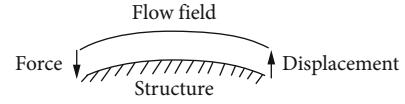

Figure 2: Coupled transfer diagram.

laminates, k_x and k_y are the bending rates of the middle surface of the laminate, and k_{xy} is the distortion rate in the middle of the laminate.

The above equation can be expressed as a matrix:

$$\begin{bmatrix} \varepsilon_x \\ \varepsilon_y \\ \gamma_{xy} \end{bmatrix} = \begin{bmatrix} \varepsilon_x^{\,0} \\ \varepsilon_y^{\,0} \\ \gamma_{xy}^{\,0} \end{bmatrix} + z \begin{bmatrix} k_x \\ k_y \\ k_{xy} \end{bmatrix}. \tag{18}$$

In the Cartesian coordinate system, the off-axis stress-strain relationship of the single-layer plate is as follows:

$$\begin{bmatrix} \sigma_x \\ \sigma_y \\ \tau_{xy} \end{bmatrix} = \begin{bmatrix} \bar{Q}_{11} & \bar{Q}_{12} & \bar{Q}_{16} \\ \bar{Q}_{12} & \bar{Q}_{22} & \bar{Q}_{26} \\ \bar{Q}_{16} & \bar{Q}_{26} & \bar{Q}_{66} \end{bmatrix}_k \begin{bmatrix} \varepsilon_x \\ \varepsilon_y \\ \gamma_{xy} \end{bmatrix}. \tag{19}$$

Among them,

$$\begin{cases} Q_{11} = \dfrac{E_1}{1 - V_{12} V_{21}}, \\ Q_{22} = \dfrac{E_2}{1 - V_{12} V_{21}}, \\ Q_{12} = \dfrac{V_{21} E_2}{1 - V_{12} V_{21}} = \dfrac{V_{12} E_1}{1 - V_{12} V_{21}}, \\ \bar{Q}_{66} = G_{12}, \end{cases} \tag{20}$$

where σ_x and σ_y are the off-axis normal stresses, τ_{xy} is the partial shear stress, ε_x and ε_y are the off-axis normal strains, γ_{xy} is the off-axis shear strain, E_1 is the longitudinal modulus of elasticity, E_2 is the transverse modulus of elasticity, G_{12} is shear elastic modulus, V_{12} is the longitudinal Poisson's ratio, V_{21} is the transverse Poisson's ratio, and $\bar{\mathbf{Q}}$ is the transformation matrix of reduced stiffness matrix **Q**, which is expressed as follows:

$$\bar{\mathbf{Q}} = \mathbf{T}^{-1} \mathbf{Q} \left(\mathbf{T}^{-1} \right)^T, \tag{21}$$

where **T** is the transpose matrix:

$$\mathbf{T} = \begin{bmatrix} \cos^2\theta & \sin^2\theta & 2\cos\theta\sin\theta \\ \sin^2\theta & \cos^2\theta & -2\cos\theta\sin\theta \\ -\cos\theta\sin\theta & \cos\theta\sin\theta & \cos^2\theta - \sin^2\theta \end{bmatrix}_k. \tag{22}$$

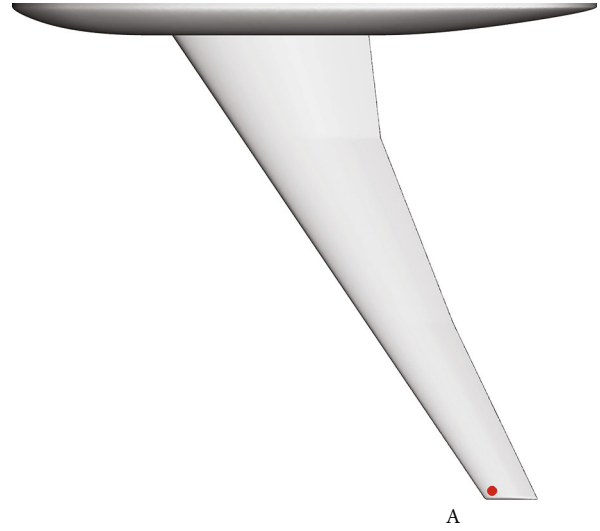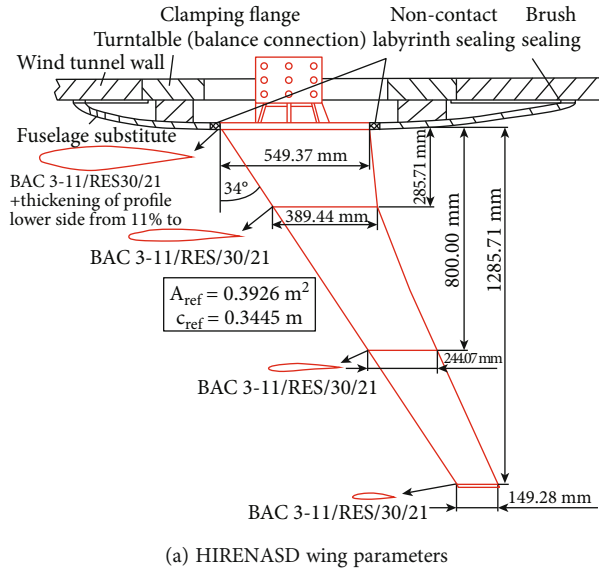(a) HIRENASD wing parameters

(b) The position of point A on the model

FIGURE 3: HIRENASD wing model and parameters.

(a) Finite element model of flow field
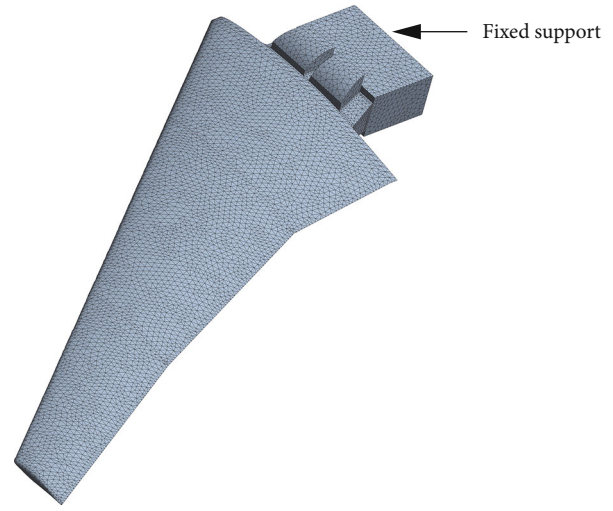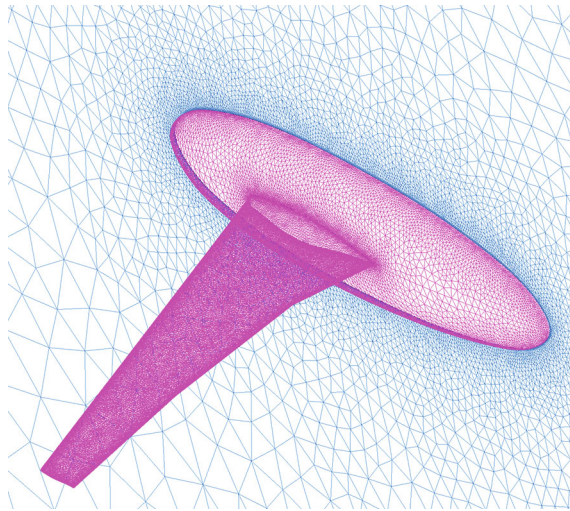

(b) Finite element model of structure

FIGURE 4: HIRENASD wing finite element model.

The stress-strain relationship of the k-layer single layer of the laminated plate in the coordinate system XYZ can be obtained by simultaneous equations (18) and (19):

$$
\begin{bmatrix} \sigma_x \\ \sigma_y \\ \tau_x \end{bmatrix} = \bar{\mathbf{Q}}_{\mathbf{k}} \left(\begin{bmatrix} \varepsilon_x^{\ 0} \\ \varepsilon_y^{\ 0} \\ \gamma_{xy}^{\ 0} \end{bmatrix} + z \begin{bmatrix} k_x \\ k_y \\ k_{xy} \end{bmatrix} \right). \tag{23}
$$

By integrating the stress of each single-layer plate, the internal force of the laminated plate can be expressed as

follows:

$$
\begin{bmatrix} N_x \\ N_y \\ N_{xy} \end{bmatrix} = \sum_{k=1}^{n} \int_{zk-1}^{zk} \begin{bmatrix} \sigma_x \\ \sigma_y \\ \tau_{xy} \end{bmatrix}_k dz = \sum_{k=1}^{n} \int_{zk-1}^{zk} \bar{\mathbf{Q}}_{\mathbf{k}} \left(\begin{bmatrix} \varepsilon_x^{\ 0} \\ \varepsilon_y^{\ 0} \\ \gamma_{xy}^{\ 0} \end{bmatrix} + z \begin{bmatrix} k_x \\ k_y \\ k_{xy} \end{bmatrix} \right) dz,
$$

$$
\begin{bmatrix} M_x \\ M_y \\ M_{xy} \end{bmatrix} = \sum_{k=1}^{n} \int_{zk-1}^{zk} \begin{bmatrix} \sigma_x \\ \sigma_y \\ \tau_{xy} \end{bmatrix}_k zdz = \sum_{k=1}^{n} \int_{zk-1}^{zk} \bar{\mathbf{Q}}_{\mathbf{k}} \left(\begin{bmatrix} \varepsilon_x^{\ 0} \\ \varepsilon_y^{\ 0} \\ \gamma_{xy}^{\ 0} \end{bmatrix} + z \begin{bmatrix} k_x \\ k_y \\ k_{xy} \end{bmatrix} \right) zdz,
$$

$$\tag{24}$$

where n is the number of single-layer plates and $zk-1$
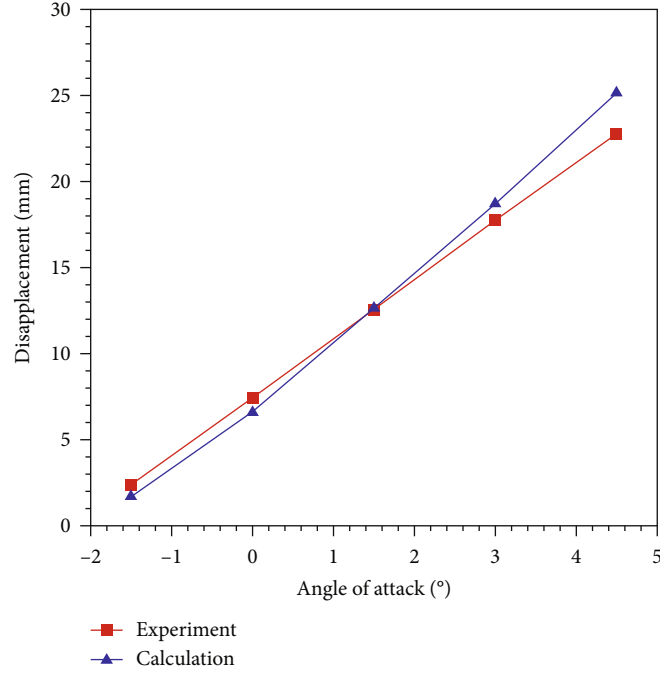
FIGURE 5: Comparison of calculated results and experimental results.

and zk are the z coordinates of the bottom and top surfaces of the single-layer plate of layer k, respectively.

Finally, the expression of internal force of composite laminates is arranged into a matrix form:

$$
\begin{bmatrix} N_x \\ N_y \\ N_{xy} \\ M_x \\ M_y \\ M_{xy} \end{bmatrix} = \begin{bmatrix} A_{11} & A_{12} & A_{16} & B_{11} & B_{12} & B_{16} \\ A_{12} & A_{22} & A_{26} & B_{12} & B_{22} & B_{26} \\ A_{16} & A_{26} & A_{66} & B_{16} & B_{26} & B_{66} \\ B_{11} & B_{12} & B_{16} & D_{11} & D_{12} & D_{16} \\ B_{12} & B_{22} & B_{26} & D_{12} & D_{22} & D_{26} \\ B_{16} & B_{26} & B_{66} & D_{16} & D_{26} & D_{66} \end{bmatrix} \begin{bmatrix} \varepsilon_x^0 \\ \varepsilon_y^0 \\ \gamma_{xy}^0 \\ k_x \\ k_y \\ k_{xy} \end{bmatrix}.
\tag{25}
$$

Among them,

$$
\begin{cases}
A_{ij} = \sum_{k=1}^{n} \left(\bar{Q}_{ij} \right)_k (z_k - z_{k-1}), \\[2mm]
B_{ij} = \frac{1}{2} \sum_{k=1}^{n} \left(\bar{Q}_{ij} \right)_k (z_k^2 - z_{k-1}^2), \\[2mm]
B_{ij} = \frac{1}{3} \sum_{k=1}^{n} \left(\bar{Q}_{ij} \right)_k (z_k^3 - z_{k-1}^3),
\end{cases}
\tag{26}
$$

where A_{11}, A_{12}, and A_{22} are the stiffness coefficients between tensile (compressive) force and middle plane tensile (compressive) strain. A_{66} is the stiffness coefficient between the shear force and the shear strain in the middle plane. A_{12} and A_{26} are the coupling stiffness coefficients between shear and tension. B_{11}, B_{12}, and B_{22} are the coupling stiffness coef-

TABLE 1: Geometrical parameters and airfoil parameters.

Parameters	Value
Half span $b/2$	16 m
Aspect ratio λ	20.65
Taper ratio η	3.4
Leading chord sweep χ_Θ	6°

ficients between tensile and bending. B_{66} is the coupling stiffness coefficient between shear and torsion. B_{12} and B_{26} are the coupling stiffness coefficients between tension and torsion or between shear and bending. D_{11}, D_{12}, and D_{22} are the stiffness coefficients between bending and bending rate. D_{66} is the coupling stiffness coefficient between torsion and torsion rate. D_{12} and D_{26} are the coupling stiffness coefficients between torsion and bending.

2.6. Validation of Calculation Methods. The HIRENASD wing model was selected as the research object (the wing model is shown in Figure 3 [40]), and the loose coupling unidirectional fluid-solid coupling theory was adopted as the calculation method [41]. The airfoil is supercritical BAC3-11/R ES/30/21, the reference area of the airfoil is 0.3926 m², the reference length is 0.3445 m, and the aspect ratio is 12.08. The longitudinal deformations of point A near the leading edge of the wingtip at angles of attack of -1.5°, 0°, 1.5°, 3°, and 4.5°, with a Reynolds number of 7×10^6 and a flight speed of 0.8 Mach were calculated, respectively.

The unstructured tetrahedral mesh was used to divide the flow field, and the mesh at the leading edge of the wing was encrypted. A total of 2,581,247 nodes and 1,869,810 grid cells were generated. The plane of the fuselage root is set as
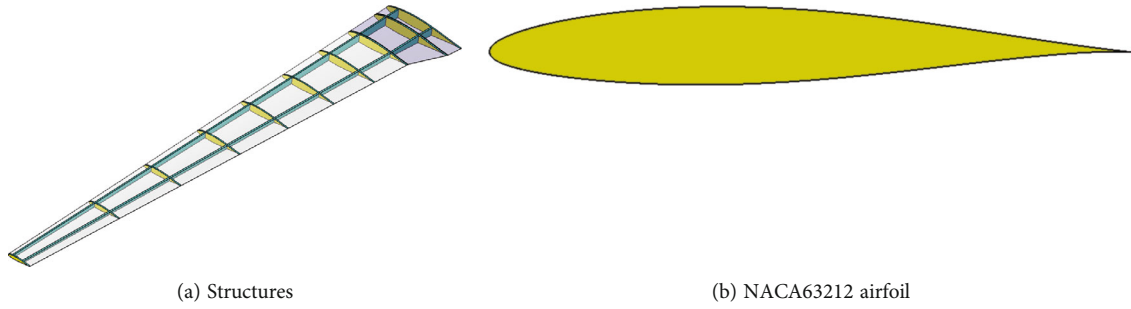
(a) Structures   (b) NACA63212 airfoil

FIGURE 6: Wing structure and airfoil profile.

TABLE 2: UT700 material parameters.

Density (kg·m³)	Elastic modulus (GPa)			Shear modulus (GPa)			Poisson's ratio		
	E_x	E_y	E_z	G_{xy}	G_{yz}	G_{xz}	PR_{xy}	PR_{xy}	PR_{xy}
1800	115	6.43	6.43	6	6	6	0.28	0.34	0.28
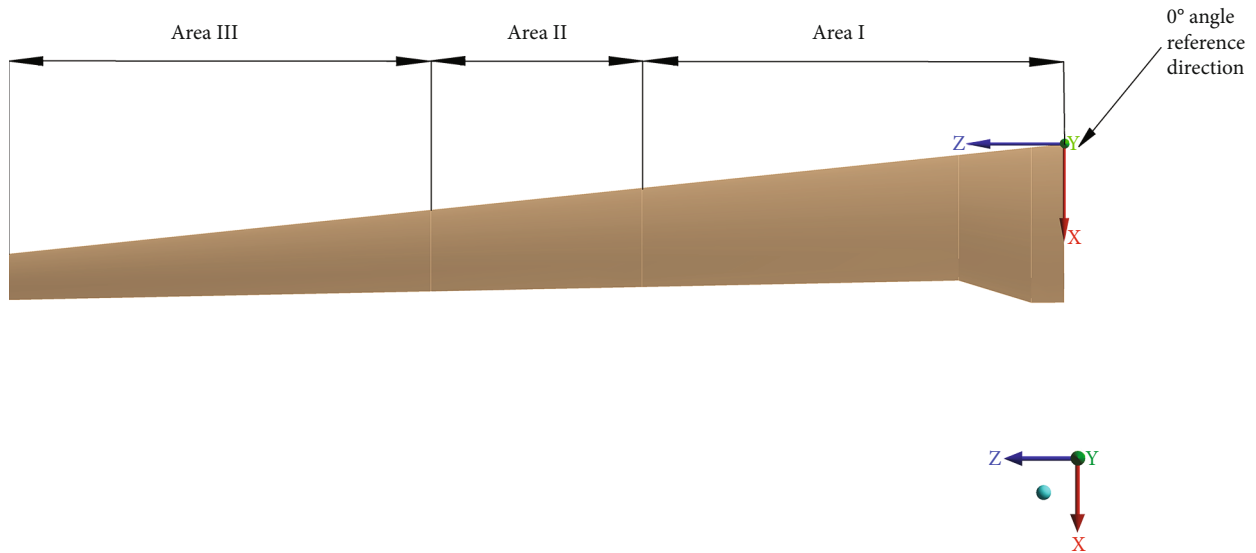
FIGURE 7: Definition of layup area and reference direction.

the symmetric boundary condition, the wing and fuselage are set as the material boundary condition, and the others are set as the far-field pressure boundary condition. In the structural calculation, the main wing finite element model was divided by unstructured tetrahedral mesh, with a total of 133,215 nodes and 75,790 mesh elements generated. The boundary condition was the constraint of the wing root fixed support. The overall meshing details are shown in Figure 4.

After calculation, the numerical simulation results agree with the experimental ones. When the angle of attack is 4.5°, there is a big difference, the maximum deformation of the test value is 25.1433 mm, the maximum deformation of the calculated value is 22.751 mm, and the deviation between the two is about 10%. The reason for the small deviation in the overall calculation may be that the deformation marks of the wing structure in the test and the deformation calculation points of the numerical calculation model cannot coincide in a strict sense, so there is a certain numerical devi-

ation. In addition, with the gradual increase of the angle of attack of the wing, the flow separation caused by the wing surface becomes more and more obvious, and the computational grid is difficult to accurately solve, so the data also produce a certain deviation. In conclusion, this method has a high simulation accuracy within a certain angle of attack calculation range and is suitable for the static aeroelastic analysis of high aspect ratio wing. Specific experimental values can be referred to References [40, 42]. Figure 5 shows the comparison between the calculated results and the simulation results.

3. Computational Model

3.1. Geometric and Material Parameters. In this paper, the wing of Global Hawk UAV is taken as the research object, and the wing mounting angle is not considered temporarily. The wing structure is a classic double-beam, multiribbed,

TABLE 3: Equal thickness layup scheme.

Unbalanced coefficient	Layer	Thickness	Layer order
0.2	40	8.0 mm	$[45°/0°/45°/0°/-45°_2/0°_2/-45°/0°_2/-45°_2/0°_2/-45°/0°/-45°/0°/-45°]_s$
0.3	40	8.0 mm	$[45°/0°/45°/0°/45°/-45°/0°_2/-45°/0°_2/-45°/0°_2/-45°/0°/-45°/0°/-45°]_s$
0.4	40	8.0 mm	$[45°/0°/45°/0°/45°_2/0°_2/-45°/0°_2/-45°/0°_2/-45°/0°/-45°/0°/-45°]_s$
0.5	40	8.0 mm	$[45°/0°/45°/0°/45°_2/0°_2/45°/0°_2/-45°/0°_2/-45°/0°/-45°/0°/-45°]_s$
0.6	40	8.0 mm	$[45°/0°/45°/0°/45°_2/0°_2/45°/0°_2/45°/-45°/0°_2/-45°/0°/-45°/0°/-45°]_s$
0.7	40	8.0 mm	$[45°/0°/45°/0°/45°_2/0°_2/45°/0°_2/45°_2/0°_2/-45°/0°/-45°/0°/-45°]_s$
0.8	40	8.0 mm	$[45°/0°/45°/0°/45°_2/0°_2/45°/0°_2/45°_2/0°_2/45°/0°/-45°/0°/-45°]_s$

TABLE 4: Variable thickness layout scheme.

Unbalanced coefficient	Area	Layer	Thickness	Layer order
	I	40	8.0 mm	$[45°/0°/45°/0°/-45°_2/0°_2/-45°/0°_2/-45°_2/0°_2/-45°/0°/-45°/0°/-45°]_s$
0.2	II	36	7.2 mm	$[45°/0°/45°/0°/-45°/0°/-45°/0°/-45°/0°/-45°/0°/-45°/0°/-45°_2]_s$
	III	32	6.4 mm	$[45°_2/0°/-45°/0°/-45°_2/0°/-45°/0°/-45°/0°/-45°/0°/-45°_2]_s$
	I	40	8.0 mm	$[45°/0°/45°/0°/45°/-45°/0°_2/-45°/0°_2/-45°_2/0°_2/-45°/0°/-45°/0°/-45°]_s$
0.3	II	36	7.2 mm	$[45°/0°/45°/0°/45°/0°/-45°/0°/-45°/0°/-45°/0°/-45°/0°/-45°_2]_s$
	III	32	6.4 mm	$[45°_2/0°/45°/0°/-45°_2/0°/-45°/0°/-45°/0°/-45°/0°/-45°_2]_s$
	I	40	8.0 mm	$[45°/0°/45°/0°/45°/45°/0°_2/-45°/0°_2/-45°_2/0°_2/-45°/0°/-45°/0°/-45°]_s$
0.4	II	36	7.2 mm	$[45°/0°/45°/0°/45°/0°/45°/0°/-45°/0°/-45°/0°/-45°/0°/-45°_2]_s$
	III	32	6.4 mm	$[45°_2/0°/45°/0°/45°/-45°/0°/-45°/0°/-45°/0°/-45°/0°/-45°_2]_s$
	I	40	8.0 mm	$[45°/0°/45°/0°/45°/45°/0°_2/45°/0°_2/-45°_2/0°_2/-45°/0°/-45°/0°/-45°]_s$
0.5	II	36	7.2 mm	$[45°/0°/45°/0°/45°/0°/45°/0°/45°/0°/-45°/0°/-45°/0°/-45°/0°/-45°_2]_s$
	III	32	6.4 mm	$[45°_2/0°/45°/0°/45°_2/0°/-45°/0°/-45°/0°/-45°/0°/-45°_2]_s$
	I	40	8.0 mm	$[45°/0°/45°/0°/45°/45°/0°_2/45°/0°_2/45°/-45°/0°_2/-45°/0°/-45°/0°/-45°]_s$
0.6	II	36	7.2 mm	$[45°/0°/45°/0°/45°/0°/45°/0°/45°/0°/45°/0°/-45°/0°/-45°/0°/-45°_2]_s$
	III	32	6.4 mm	$[45°_2/0°/45°/0°/45°_2/0°/45°/0°/-45°/0°/-45°/0°/-45°_2]_s$
	I	40	8.0 mm	$[45°/0°/45°/0°/45°/45°/0°_2/45°/0°_2/45°_2/0°_2/-45°/0°/-45°/0°/-45°]_s$
0.7	II	36	7.2 mm	$[45°/0°/45°/0°/45°/0°/45°/0°/45°/0°/45°/0°/-45°/0°/-45°_2]_s$
	III	32	6.4 mm	$[45°_2/0°/45°/0°/45°_2/0°/45°/0°/45°/0°/-45°/0°/-45°_2]_s$
	I	40	8.0 mm	$[45°/0°/45°/0°/45°/45°/0°_2/45°/0°_2/45°_2/0°_2/45°/0°/-45°/0°/-45°]_s$
0.8	II	36	7.2 mm	$[45°/0°/45°/0°/45°/0°/45°/0°/45°/0°/45°/0°/45°/0°/-45°_2]_s$
	III	32	6.4 mm	$[45°_2/0°/45°/0°/45°_2/0°/45°/0°/45°/0°/45°/0°/-45°_2]_s$

upper and lower skin structure. The airfoil is NACA63212 laminar flow airfoil with a flight altitude of 15,000 meters, angle of attack is 2°, and a flight speed of 0.6 Mach when cruising. The specific parameters of the wing are shown in Table 1, and the structure and wing profile are shown in Figure 6.

The mechanical characteristics of the wing with high aspect ratio are that the bending moment at the wing root is relatively large, and the wing surface is prone to combined deformation of bending and torsion. According to the above characteristics, the reasonable application of composite materials can significantly improve the performance of the

structure. Based on the above viewpoints, the wing skin was laminated with composite materials. Among them, the wing SPAR and wing ribs are made of aluminum alloy, the yield limit is 280 MPa, the safety factor is 2, the Young's modulus of elasticity is 71 GPa, and the Poisson's ratio is 0.33. UT700 is selected as the laminating material, and the specific material parameters are shown in Table 2.

3.2. Layout Design. In the layup area, layup area I was defined as 40% and half of the wingspan along the wing root as the starting point, layup area II was defined as 20% of the extension along the wing tip, and layup area III was defined

TABLE 5: Variable thickness and angle layup scheme.

Unbalanced coefficient	Area	Layer	Thickness	Layer order
	I	40	8.0 mm	$[45°/0°/45°/0°/-45°_2/0°/90°/-45°/90°_2/-45°_2/90°_2/-45°/0°/-45°/0°/-45°]_s$
0.2	II	36	7.2 mm	$[45°/0°/45°/0°/-45°/90°/-45°/90°/-45°/90°/-45°/90°/-45°/0°/-45°/0°/-45°_2]_s$
	III	32	6.4 mm	$[45°_2/0°/-45°/0°/-45°_2/90°/-45°/90°/-45°/90°/-45°/0°/-45°_2]_s$
	I	40	8.0 mm	$[45°/0°/45°/0°/45°/-45°/0°/90°/-45°/90°_2/-45°_2/90°_2/-45°/0°/-45°/0°/-45°]_s$
0.3	II	36	7.2 mm	$[45°/0°/45°/0°/45°/90°/-45°/90°/-45°/90°/-45°/90°/-45°/0°/-45°/0°/-45°_2]_s$
	III	32	6.4 mm	$[45°_2/0°/45°/0°/-45°_2/90°/-45°/90°/-45°/90°/-45°/90°/-45°_2]_s$
	I	40	8.0 mm	$[45°/0°/45°/0°/45°/45°/0°/90°/-45°/90°_2/-45°_2/90°_2/-45°/0°/-45°/0°/-45°]_s$
0.4	II	36	7.2 mm	$[45°/0°/45°/0°/45°/90°/45°/90°/-45°/90°/-45°/90°/-45°/0°/-45°/0°/-45°_2]_s$
	III	32	6.4 mm	$[45°_2/0°/45°/0°/45°/-45°/90°/-45°/90°/-45°/90°/-45°/0°/-45°_2]_s$
	I	40	8.0 mm	$[45°/0°/45°/0°/45°_2/0°/90°/45°/90°_2/-45°_2/90°_2/-45°/0°/-45°/0°/-45°]_s$
0.5	II	36	7.2 mm	$[45°/0°/45°/0°/45°/90°/45°/90°/45°/90°/-45°/90°/-45°/0°/-45°/0°/-45°_2]_s$
	III	32	6.4 mm	$[45°_2/0°/45°/0°/45°_2/90°/-45°/90°/-45°/90°/-45°/0°/-45°_2]_s$
	I	40	8.0 mm	$[45°/0°/45°/0°/45°_2/0°/90°/45°/90°_2/45°/-45°/90°_2/-45°/0°/-45°/0°/-45°]_s$
0.6	II	36	7.2 mm	$[45°/0°/45°/0°/45°/90°/45°/90°/45°/90°/45°/90°/-45°/0°/-45°/0°/-45°_2]_s$
	III	32	6.4 mm	$[45°_2/0°/45°/0°/45°_2/90°/45°/90°/-45°/90°/-45°/0°/-45°_2]_s$
	I	40	8.0 mm	$[45°/0°/45°/0°/45°_2/0°/90°/45°/90°_2/45°_2/90°_2/-45°/0°/-45°/0°/-45°]_s$
0.7	II	36	7.2 mm	$[45°/0°/45°/0°/45°/90°/45°/90°/45°/90°/45°/90°/45°/0°/-45°/0°/-45°_2]_s$
	III	32	6.4 mm	$[45°_2/0°/45°/0°/45°_2/90°/45°/90°/45°/90°/-45°/0°/-45°_2]_s$
	I	40	8.0 mm	$[45°/0°/45°/0°/45°_2/0°/90°/45°/90°_2/45°_2/90°_2/45°/0°/-45°/0°/-45°]_s$
0.8	II	36	7.2 mm	$[45°/0°/45°/0°/45°/90°/45°/90°/45°/90°/45°/90°/45°/0°/45°/0°/-45°_2]_s$
	III	32	6.4 mm	$[45°_2/0°/45°/0°/45°_2/90°/45°/90°/45°/90°/45°/0°/-45°_2]_s$

as the rest of the wingtip. The reference direction is the normal direction of the wing root plane. The specific division of layering area is shown in Figure 7.

In layup design, in order to study the influence of the ratio of unbalanced coefficient on the layup wing structure, under the condition of gradually adjusting the unbalanced coefficient, the maximum wing tip displacements of 0° and ±45° lamination under constant thickness lamination and variable thickness lamination were studied, respectively. The maximum wing tip displacements with varying thickness and angle and varying thickness and angle are studied by adding the layup angle of 90°.

In the case of constant thickness layup, it is assumed that the initial thickness of all-aluminum wing skin is 8 mm and the thickness of laminated plate is 0.2 mm per layer. Then, the reference composite layup scheme is shown in Table 3.

In the layer with variable thickness, the proportion of 0° in each area was changed, and the size of the control unbalanced coefficient remained basically unchanged. The thickness at the wing root is the largest and gradually decreases along the span direction to the wing tip. The specific layup scheme is shown in Table 4.

After adding 90° layup angle on the basis of variable thickness layup, the proportion of 0° layup angle in the overall layup angle will be reduced accordingly. Controlling 0° and 90° in each layer of the same proportion, both are

50%. At the same time, the size of the unbalanced coefficient is basically unchanged. The specific layup scheme is shown in Table 5.

Finally, under the condition of changing the unbalanced coefficient, it is assumed that the layup angles of 90° are fixed four. When four 90° I layer angle is located in the area, is the area I orientations of 0°, ±45°, 90°, the rest of the two area layer angle only 0° and ±45°. Then the 90° layup angle is added to region II; the regions I and III are kept at 0° and ±45°, respectively. Similarly, to guarantee the area I, II is only 0° and ±45°, and area III contains added 90° laid angle. This is to determine the effect of the layup angle on each wing segment. Take the case of unbalanced coefficient 0.2 as an example, the specific scheme is shown in Table 6, and the rest of the cases are similar.

3.3. Calculation and Solution. When the aerodynamic load is calculated, the flow field is solved and calculated based on the Spalart-Allmaras turbulence model. In the spatial discrete term, the viscous flux vector is selected as the central format, and the relative flux vector is selected as the Roe-FDS format. In the time discrete term, the LU-SGS implicit time discrete method is used to advance the solution [43]. Unstructured grids are used in the flow field calculation domain and the wing, and the grids near the object surface are refined and encrypted. Combined with the actual

TABLE 6: Variable thickness and angle layup scheme example.

Unbalanced coefficient	Area	Layer	Thickness	Layer order
	I	40	8.0 mm	$[45°/0°/45°/0°/-45°_2/0°/90°/-45°/90°_2/-45°_2/90°/0°/-45°/0°/-45°/0°/-45°]_s$
0.2	II	36	7.2 mm	$[45°/0°/45°/0°/-45°/0°/-45°/0°/-45°/0°/-45°/0°/-45°/0°/-45°/0°/-45°_2]_s$
	III	32	6.4 mm	$[45°_2/0°/-45°/0°/-45°_2/0°/-45°/0°/-45°/0°/-45°/0°/-45°_2]_s$
	I	40	8.0 mm	$[45°/0°/45°/0°/-45°_2/0°_2/-45°/0°_2/-45°_2/0°/-45°/0°/-45°/0°/-45°]_s$
0.2	II	36	7.2 mm	$[45°/0°/45°/0°/-45°/90°/-45°/90°/-45°/90°/-45°/90°/-45°/0°/-45°/0°/-45°_2]_s$
	III	32	6.4 mm	$[45°_2/0°/-45°/0°/-45°_2/0°/-45°/0°/-45°/0°/-45°/0°/-45°_2]_s$
	I	40	8.0 mm	$[45°/0°/45°/0°/-45°_2/0°_2/-45°/0°_2/-45°/0°_2/-45°/0°/-45°/0°/-45°]_s$
0.2	II	36	7.2 mm	$[45°/0°/45°/0°/-45°/0°/-45°/0°/-45°/0°/-45°/0°/-45°/0°/-45°/0°/-45°_2]_s$
	III	32	6.4 mm	$[45°_2/0°/45°/90°/-45°_2/90°/-45°/90°/-45°/90°/-45°/0°/-45°_2]_s$

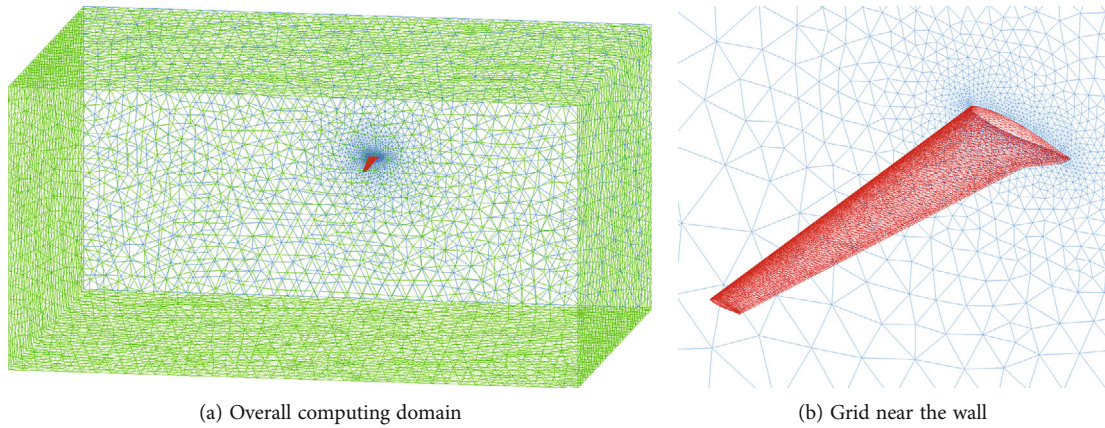(a) Overall computing domain   (b) Grid near the wall

FIGURE 8: Calculation domain and mesh of flow field.

calculation conditions and through the independent verification of grid and iteration steps, a total of 986,262 nodes and 717,173 grid cells were finally generated. The boundary conditions at the wing root are set as symmetric boundary conditions, the wing surface is set as object surface boundary conditions, and the rest are set as far-field boundary conditions of pressure. The grid division of the computational domain of the wing flow field is shown in Figure 8.

Considering the influence of geometric nonlinearity, the Newton-Raphson iterative method is used for numerical analysis of structural deformation [44]. The wing finite element structure model was divided by unstructured tetrahedral mesh, and the wing root was applied with fixed constraints. A total of 121,171 nodes and 86,675 mesh elements were obtained. Secondly, the aerodynamic loads solved in the above flow fields are interpolated to the nodes of the structural grid. The specific grid partitioning and aerodynamic interpolation are shown in Figure 9.

4. Result Analysis

4.1. The Relation between Unbalanced Coefficient and Thickness. Figure 10 shows the variation relationship between the unbalanced coefficient and the wing tip displacement. With the increase of the unbalanced coefficient,

the wingtip displacement first decreases and then increases, and presents a symmetric trend along the unbalanced coefficient of 0.5 (i.e., symmetric layup). When the unbalanced coefficient is 0.5, the structural deformation is the least. Secondly, in this example, the maximum wing tip displacement calculated in the case of constant thickness layup is similar to that in the case of variable thickness layup. The distributions of the longitudinal displacements and the broad-span displacements at the leading edge of the wing are basically the same, which is due to the small variation of the gradient with variable thickness. The distribution of chord displacement is different with the change of unbalanced coefficient.

When the unbalanced coefficient is 0.3, it shows a linear deformation relationship along the wingspan under constant thickness and variable thickness. When the unbalanced coefficient is 0.5 and 0.7, the chord deformation no longer obeys the linear relationship, and its change situation increases first and then decreases, and the peak value of growth occurs at about half of the half-length. With the increase of the unbalanced coefficient, the chordal displacement of the wingtip gradually decreases. Therefore, in general composite wing skin-laying, when only 0° and ±45° lamination angles are considered, symmetrical lamination should be used as far as possible. Moreover, the thickness of lamination varies
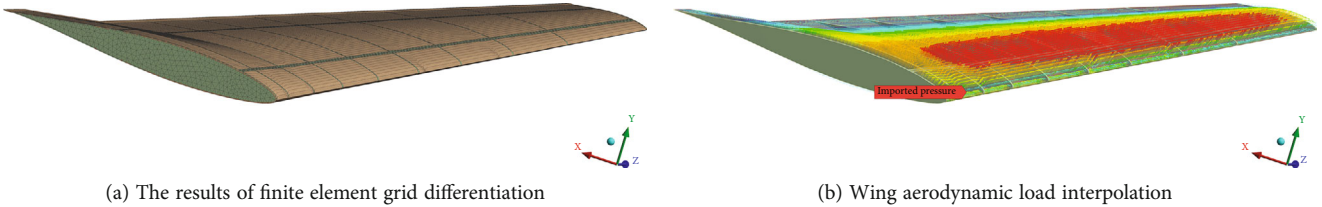
(a) The results of finite element grid differentiation

(b) Wing aerodynamic load interpolation

FIGURE 9: Mesh partitioning and aerodynamic interpolation results.

(a) Maximum wing displacement

(b) Variation of leading edge longitudinal displacement

(c) Variation of leading edge wingspan displacement

(d) Variation of leading edge chordal displacement
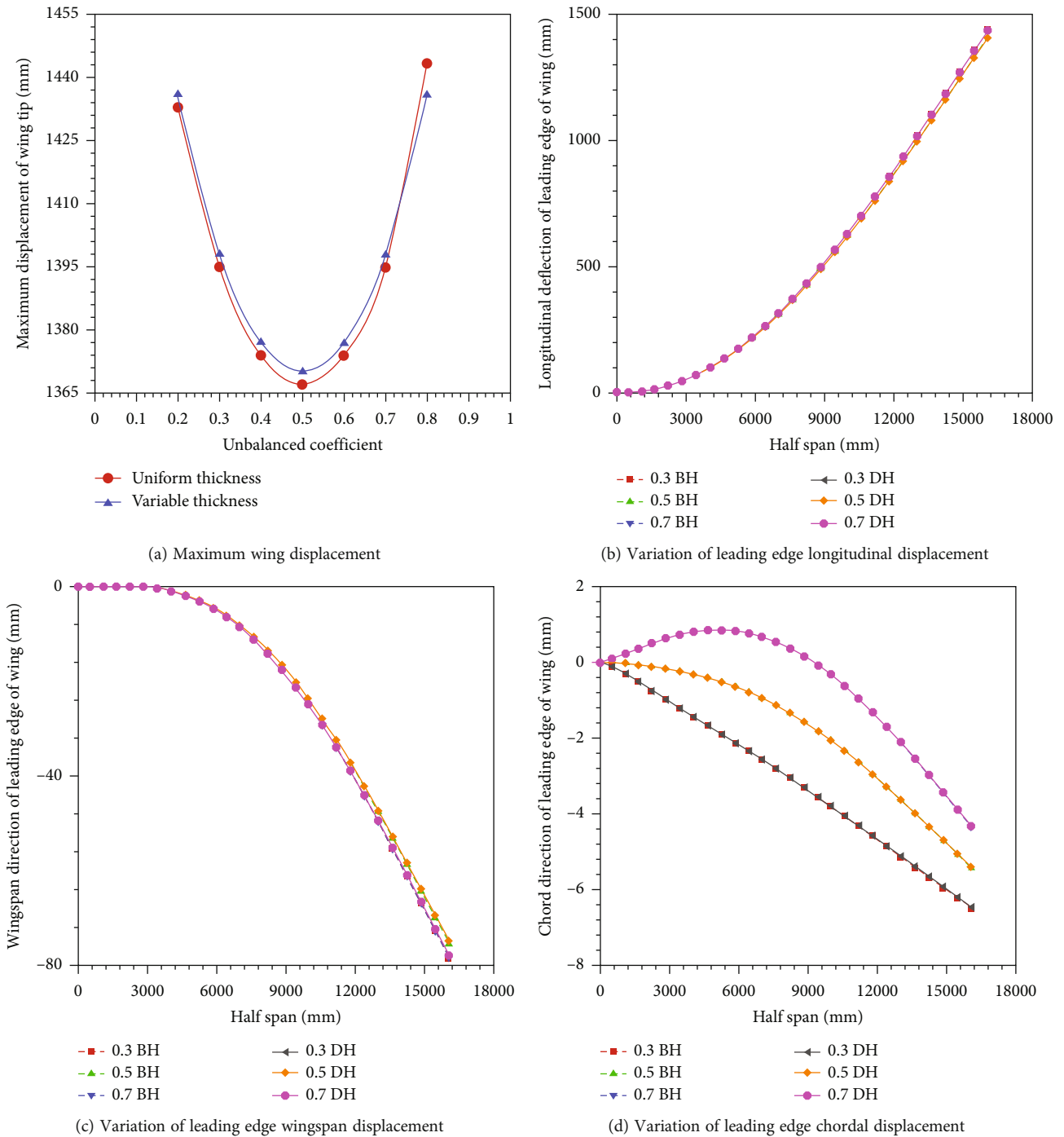
FIGURE 10: Deformation of airfoil with changing thickness layup.

(a) Maximum wing displacement

(b) Variation of leading edge longitudinal displacement

(c) Variation of leading edge wingspan displacement

(d) Variation of leading edge chordal displacement
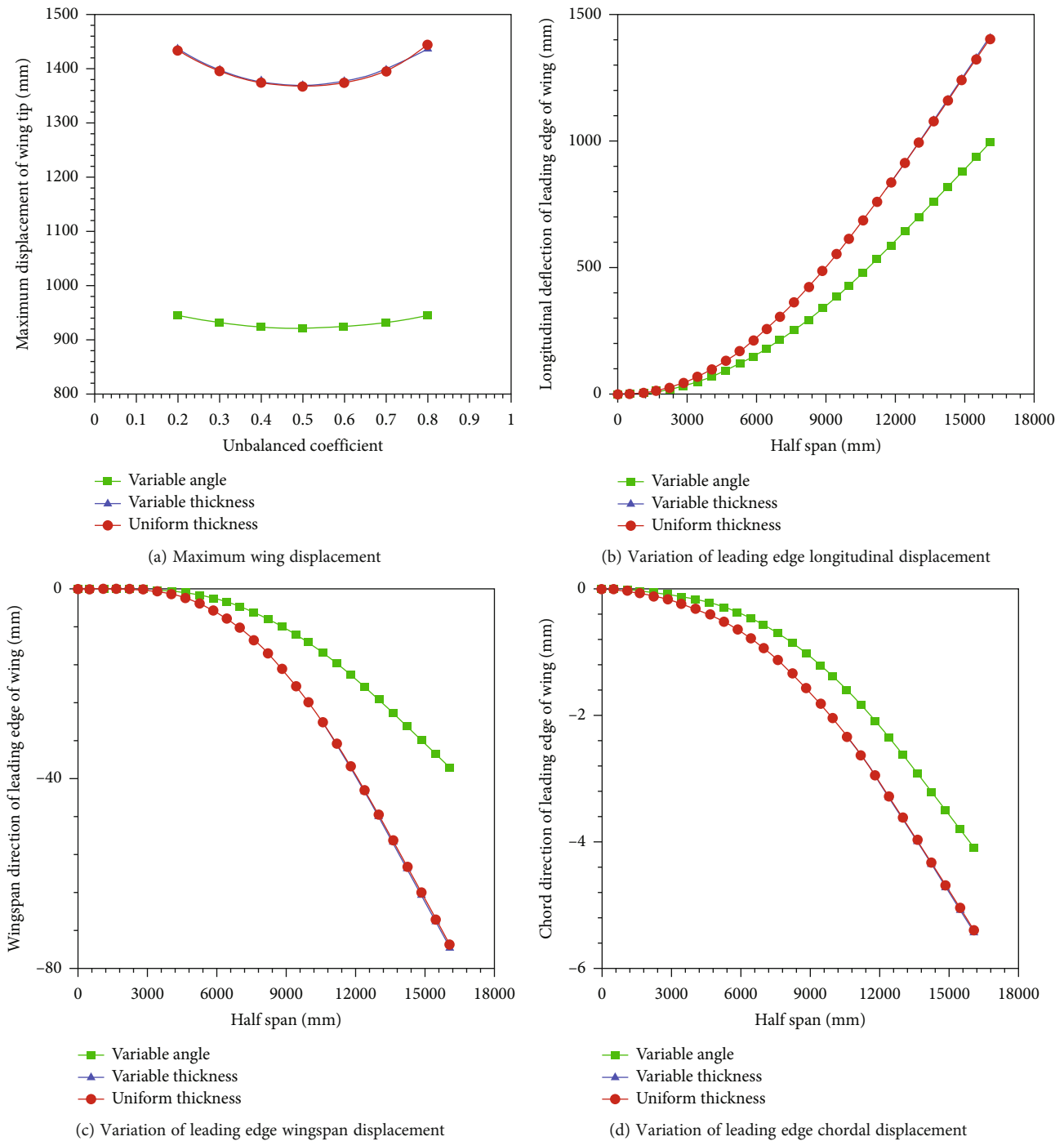
FIGURE 11: Deformation of the wing with the addition of angle layering.

slightly along the span direction, so variable thickness lamination should be used to reduce the weight of wing structure.

4.2. The Relation between Unbalanced Coefficient and Angle. The influence of unbalanced coefficient and lamination angle on structural deformation is shown in Figure 11. The maximum displacement of the wing structure is significantly reduced by adding 90° layup angle. Similarly, after adding the layup angle of 90°, the overall deformation still obeys

the law of symmetrical distribution. When the unbalanced coefficient is 0.5, the maximum displacement of the wing tip is the smallest, and the displacements under the other coefficients are symmetrically distributed with the unbalanced coefficient of 0.5. Taking the unbalanced coefficient 0.5 as an example, the influence of the change of the unbalanced coefficient on the wing displacement in all directions is shown in Figures 10(b)–10(d).

The significant reduction of displacement is due to the fact that the original laminates laid at 0° and ±45° only

(a) Maximum wing displacement

(b) Variation of leading edge longitudinal displacement

(c) Variation of leading edge wingspan displacement

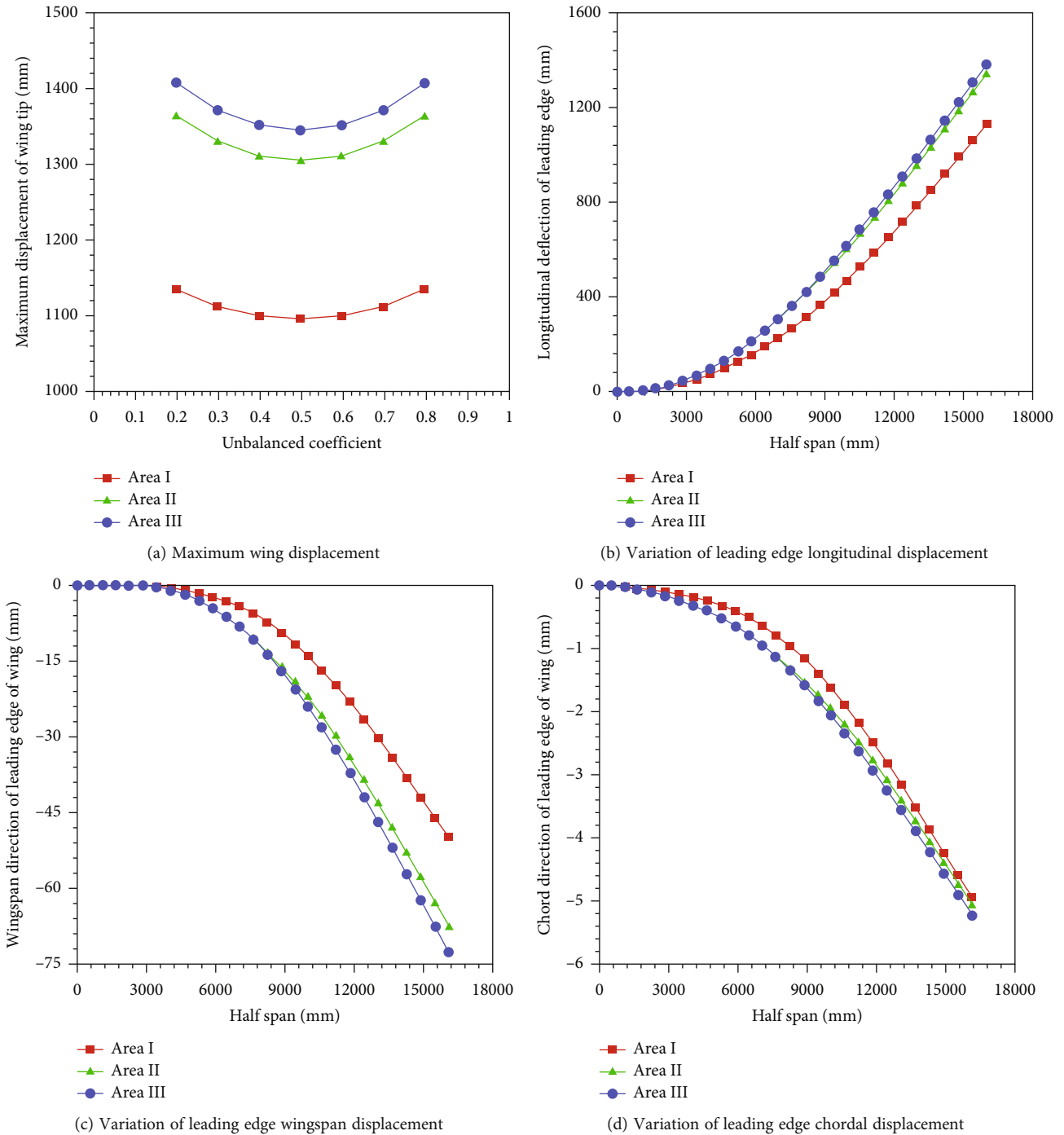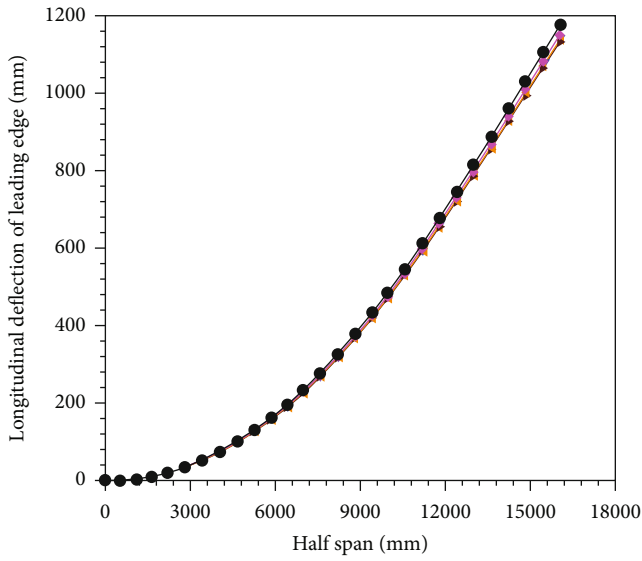(d) Variation of leading edge chordal displacement

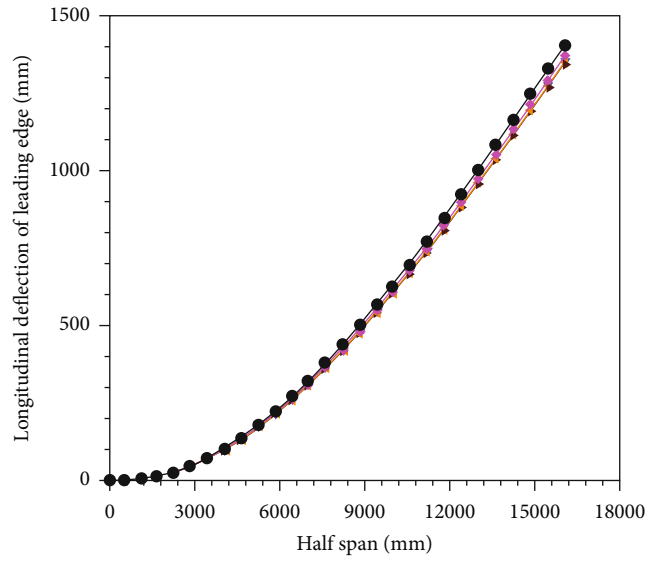FIGURE 12: Influence of laminated area on wing deformation.

provide directional tensile and shear strength, and the addition of additional 90° laminates along different directions can produce quasi-isotropic laminates. Compared with the laminates with 0° and ±45°, the multiangle composite laminates with 90° have stronger deformation-resistant and damage-resistant abilities. Therefore, the multiangle composite laminates have stronger resistance to deformation than the double-angle laminates.

4.3. The Relation between Unbalanced Coefficient and Layup Area. The size of unbalanced coefficient and the selection of layup angle have different effects on different layup areas. As shown in Figure 12, taking the unbalanced coefficient of 0.5 as an example, the outermost segment of the wing has the largest deformation, while the innermost segment of the wing has the smallest deformation. The influence of the change of the unbalanced coefficient on the lamination area
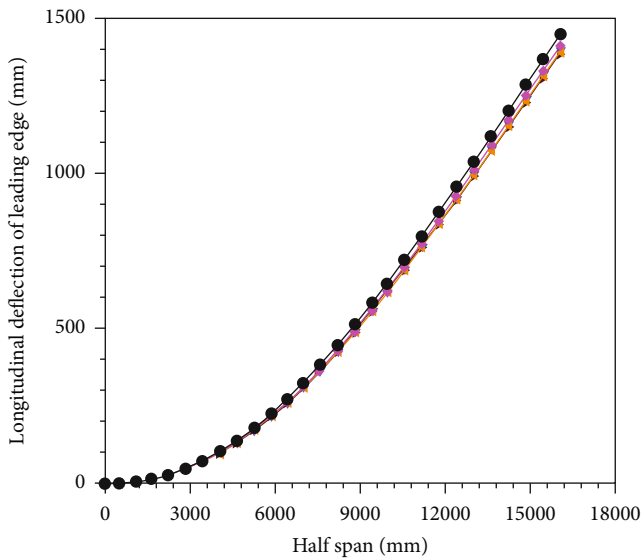
(a) Leading edge longitudinal displacement in area I

(b) Leading edge longitudinal displacement in area II

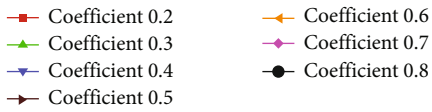

(c) Leading edge longitudinal displacement in area III

(d) Leading edge wingspan displacement in area I

FIGURE 13: Continued.
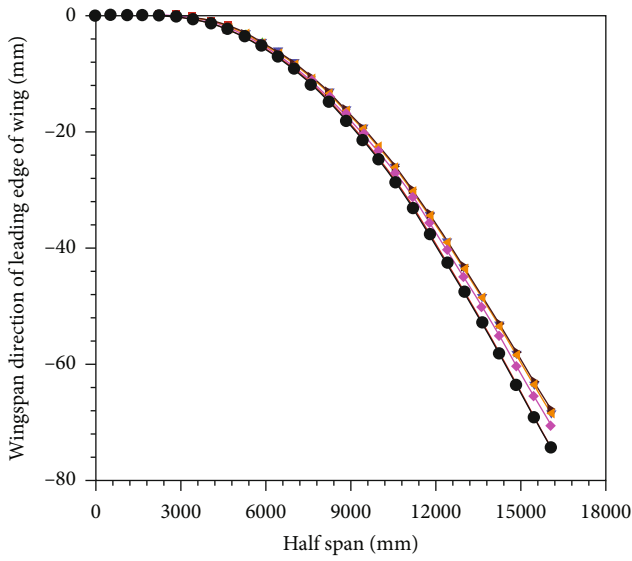
(e) Leading edge wingspan displacement in area II
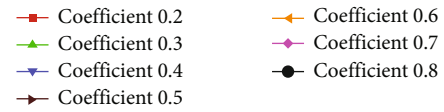
(f) Leading edge wingspan displacement in area III

(g) Leading edge chord displacement in area I

(h) Leading edge chord displacement in area II
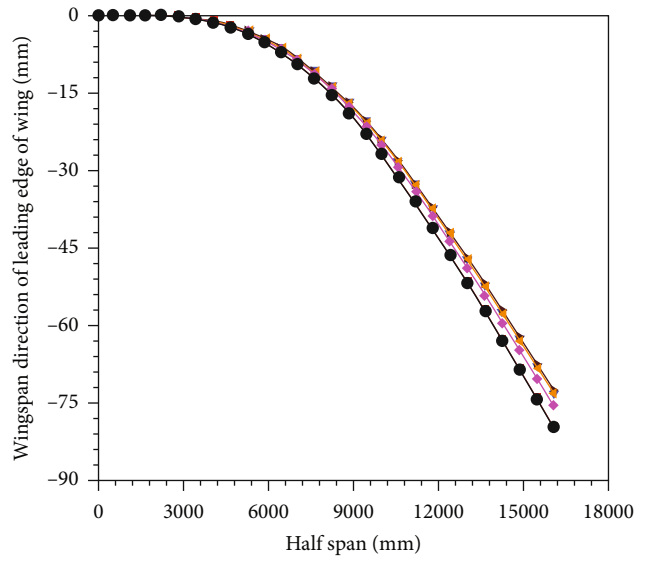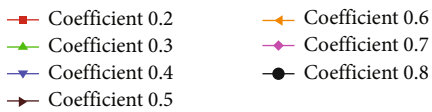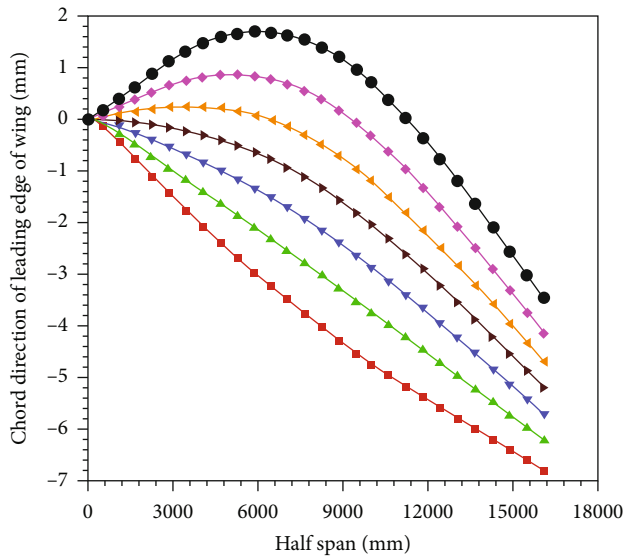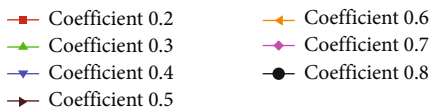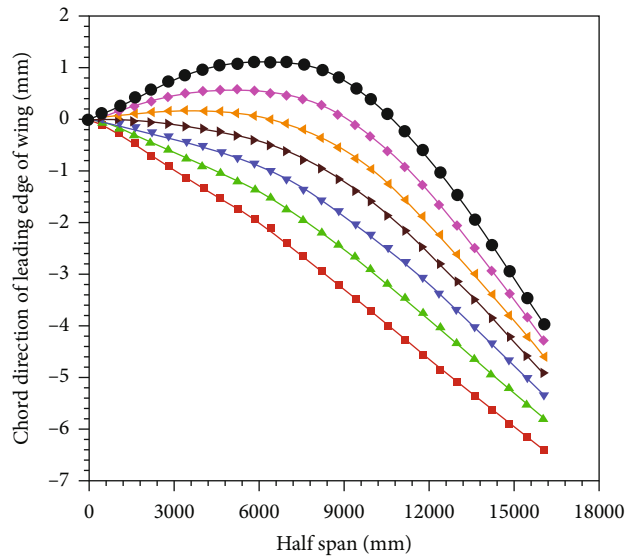
FIGURE 13: Continued.
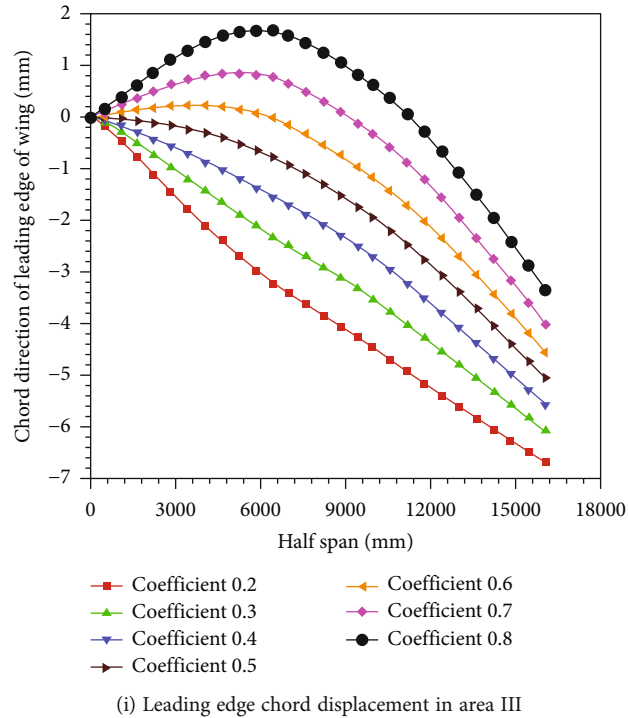
(i) Leading edge chord displacement in area III

FIGURE 13: Displacement comparison in different directions in each laminated area.

III is smaller and larger than that of the lamination area. Compared with the general wing, the high aspect ratio wing has greater flexibility and lower stiffness, so the influence of geometric nonlinearity cannot be ignored. The layup area III is located at the outer end of the wing, and the geometric deformation is relatively larger, so after the composite layup design, there is a more obvious deformation change.

Figure 13, respectively, shows the displacement changes in all directions in the layup area I, and tunnel with the change of the unbalanced coefficient. Figures 13(a)–13(c) describe the longitudinal displacement of the wing under the change of the unbalanced coefficient. The maximum vertical displacement in the laying area I is 1176.6 mm, and the maximum vertical displacement in the laying area is 1407.8 mm and 1454.4 mm, respectively. The difference between the two is small. Secondly, when the unbalanced coefficient is 0.8 or 0.2 in all the bedding areas, the displacement reaches the maximum. When the unbalanced coefficient is 0.5, its displacement reaches the minimum value. Figures 13(d)–13(f) describe the variation of displacement in the spreading direction of each laminated area. The maximum displacement in the spreading direction of the bedding area I is -53.9 mm, the maximum displacement in the spreading direction of the bedding area is -74.5 mm, and the maximum displacement in the spreading direction of the bedding area is -79.9 mm. The variation rule is basically the same as that in the longitudinal direction, but the spanwise displacement when the unbalanced coefficient is 0.8 is slightly larger than that when the unbalanced coefficient is 0.2. Figures 13(g)–13(i) show that the chord direction wing displacement changes with the change of the layup area. It can be seen that, compared with the longitudinal displace-

ment and the spanwise displacement, the chord direction is greatly affected by the change of the unbalanced coefficient. When the unbalanced coefficient is 0.8, as the layup area of the wing segment changes, the chordal displacement change in the layup area II is smaller than that in the layup area; that is, the chordal displacement change in the layup coupling area in the middle of the wing segment is smaller than that in the coupling area of the outer wing segment and the inner wing segment. Similarly, the unbalanced coefficient increases in the three layup regions, the chordal displacement changes from linear to nonlinear along the span direction, and the chordal deformation gradually decreases along the wing span direction. In general, the change of unbalanced coefficient has a certain influence on the division of the wing layup area. The specific causes are still under further research and exploration.

5. Conclusion

In this paper, the unidirectional fluid-structure coupling calculation method based on loose coupling is used to study the influence of the change of unbalanced coefficient on the static aeroelastic characteristics of the wing with high aspect ratio under the condition of geometric nonlinearity, and the following conclusions are drawn:

(1) There is not only a single corresponding relationship between the maximum wing deformation and the change of unbalanced coefficient. However, with the increase of the unbalanced coefficient, it shows a trend of decreasing first and then increasing. The minimum deformation of the wing occurs when

the unbalanced coefficient is 0.5 (i.e., the opposite lamination), and the deformation of the wing is symmetrically distributed on both sides when the unbalanced coefficient is 0.5

(2) When the layup angle only has 0° and ±45°, the wing deformation obtained by the two schemes is basically the same as that obtained by the same thickness layup method and the variable thickness layup method. So, in the design of wing skin layup, variable thickness layup should be adopted as far as possible, which is beneficial to the weight reduction of wing structure

(3) Compared with the double-ply angle-ply scheme, the mixed angle-ply scheme has a greater inhibition on the wing deformation. This is because the mechanical properties of laminates will be changed by multi-angle laminating, which will change the bending and torsion properties of laminates

(4) The effect of layup angle on the layup area III (outer wing section) was greater than that of the other two areas. Different wing segments have different sensibilities to the 90° layup angle. The specific layup sequence, layup angle, and the layup of wing segment should be selected according to the mission requirements of aircraft design

(5) The change of unbalanced coefficient will significantly change the chord displacement of the wing. With the increase of unbalanced coefficient, the chord displacement along the spanwise direction changes from linear distribution to nonlinear distribution. The abrupt change is generally located at the average half span of the wing, and the chordal displacement decreases along the wing span

Data Availability

The data used to support the findings of this study are available from the corresponding author upon request.

Conflicts of Interest

The authors declare that they have no conflicts of interest.

Acknowledgments

References

[1] D. U. Shanyi, "Advanced composite materials and aerospace engineering," *Acta Materiae Compositae Sinica*, vol. 24, no. 1, 2007.

[2] N. N. Ni, K. Bian, L. Xia, W. K. Gu, and Y. F. Wen, "Application of advanced composite materials for UAV," *Journal of Aeronautical Materials*, vol. 39, no. 5, pp. 45–60, 2019.

[3] C. Shaojie, "Reunite the material and the B7E7 dream airplane," *The Aviation Manufacturing Technique*, vol. 1, pp. 34–37, 2005.

[4] M. A. Limin, Z. H. A. N. G. Jiazhen, and Y. U. E. Guangquan, "Application of composites in new generation of large civil aircraft," *Acta Materiae Compositae Sinica*, vol. 32, no. 2, pp. 317–322, 2015.

[5] J. W. Xiang, Z. Kan, H. Y. Shao, H. D. Li, X. Dong, and D. C. Li, "A review of key technologies for long-endurance unmanned aerial vehicle," *Journal of Harbin Institute of Technology*, vol. 52, no. 6, pp. 57–77, 2020.

[6] Z. Wan, K. Shao, C. Yang, and K. Wang, "Aeroelastic analysis of composite wings with unbalance laminates," *Acta Materiae Compositae Sinica*, vol. 25, no. 1, pp. 196–199, 2008.

[7] L. Liang, Z. Q. Wan, and C. Yang, "Aeroelastic optimization on composite skins of large aircraft wings," *Science China Technological Sciences*, vol. 55, no. 4, pp. 1078–1085, 2012.

[8] L. Zhou, Z. Q. Wan, and C. Yang, "Effect of laminate parameters of composite skin on aeroelastic optimization of high-aspect-ratio wing," *Acta Materiae Compositae Sinica*, vol. 30, no. 5, pp. 195–200, 2013.

[9] D. W. Xu, Z. N. Li, and D. G. Cui, "Bend twist coupling effects of unsymmetric and unbalanced laminate," *Journal of Beijing University of Aeronautics and Astronautics*, vol. 27, no. 2, pp. 167–170, 2001.

[10] Z. Xingyin, A. Liqiang, and W. Zhangqi, "Bend-twist coupling effect of symmetric un-uniform laminate plate beam," *Acta Materiae Compositae Sinica*, vol. 34, no. 7, pp. 1462–1468, 2017.

[11] A. Zhang, Y. Chai, and D. Guan, "Test method for bending-twisting coupling deformation of unsymmetrical/unbalanced composite laminates," *Acta Materiae Compositae Sinica*, vol. 29, no. 1, pp. 207–211, 2012.

[12] J. Wang, S. Lei, T. Li, W. Zhang, Z. Ren, and H. Cui, "Effect of ply angle on nonlinear static aeroelasticity of high-aspect-ratio composite wing," *Journal of Vibroengineering*, vol. 22, no. 4, pp. 959–970, 2020.

[13] E. I. Basri, M. T. H. Sultan, M. Faizal et al., "Performance analysis of composite ply orientation in aeronautical application of unmanned aerial vehicle (UAV) NACA4415 wing," *Journal of Materials Research and Technology*, vol. 8, no. 5, pp. 3822–3834, 2019.

[14] R. Koohi, H. Shahverdi, and H. Haddadpour, "Nonlinear aeroelastic analysis of a composite wing by finite element method," *Composite Structures*, vol. 113, no. 1, pp. 118–126, 2014.

[15] C. C. Xie, J. Z. Lie, and C. Yang, "Geometrical nonlinear aeroelastic stability analysis of a composite high-aspect-ratio wing," *International Journal of Aerospace Engineering*, vol. 15, 333 pages, 2008.

[16] B. Kirsch, O. Montagnier, E. Bénard, and T. M. Faure, "Tightly coupled aeroelastic model implementation dedicated to fast aeroelastic tailoring optimisation of high aspect ratio composite wing," *Journal of Fluids and Structures*, vol. 94, 2020.

[17] M. Bourchak and Y. Dobah, "Design and analysis of a morphing composite airfoil using unbalanced layup and unconventional ply angles," *Transactions of the Japan Society for Aeronautical and Space Sciences*, vol. 57, no. 2, pp. 79–85, 2014.

[18] J. Dillinger, M. M. Abdalla, Y. M. Meddaikar, and T. Klimmek, "Static aeroelastic stiffness optimization of a forward swept composite wing with CFD-corrected aero loads," *CEAS Aeronautical Journal*, vol. 10, no. 4, pp. 1015–1032, 2019.

[19] Y. Yu, Z. Wang, and S. Guo, "Efficient method for aeroelastic tailoring of composite wing to minimize gust response," *International Journal of Aerospace Engineering*, vol. 2017, Article ID 1592527, 12 pages, 2017.

[20] K. Bramsiepe, A. Voß, and T. Klimmek, "Design and sizing of an aeroelastic composite model for a flying wing configuration with maneuver, gust, and landing loads," *CEAS Aeronautical Journal*, vol. 11, no. 3, pp. 677–691, 2020.

[21] S. Shrivastava, P. M. Mohite, T. Yadav, and A. Malagaudanavar, "Multi-objective multi-laminate design and optimization of a carbon fibre composite wing torsion box using evolutionary algorithm," *Composite Structures*, vol. 185, pp. 132–147, 2018.

[22] K. Sinha, T. Klimmek, M. Schulze, and V. Handojo, "Loads analysis and structural optimization of a high aspect ratio, composite wing aircraft," *CEAS Aeronautical Journal*, vol. 12, no. 2, pp. 233–243, 2021.

[23] V. Shukla and J. Singh, "Modeling and analysis of cross-ply and angle-ply laminated plates under patch loads using RBF based meshfree method and new HSDT," *Computers & Mathematics with Applications*, vol. 79, no. 8, 2020.

[24] Y. W. Kwon, "Analysis of laminated composite plates with fluid–structure interaction using multiscale modeling technique," *Multiscale and Multidisciplinary Modeling, Experiments and Design*, vol. 4, no. 1, pp. 51–63, 2021.

[25] R. Guillén-Rujano, F. Avilés, A. Vidal-Lesso, and A. Hernández-Pérez, "Closed-form solution and analysis of the plate twist test in sandwich and laminated composites," *Mechanics of Materials*, vol. 155, p. 103753, 2021.

[26] B. R. Thakur, S. Verma, B. N. Singh, and D. K. Maiti, "Geometrically nonlinear dynamic analysis of laminated composite plate using a nonpolynomial shear deformation theory," *International Journal of Non-Linear Mechanics*, vol. 128, no. 10, p. 103635, 2021.

[27] S. C. Yang and Q. S. Yang, "Geometrically nonlinear transient response of laminated plates with nonlinear elastic restraints," *International Journal of Structural Stability and Dynamics*, vol. 2017, article 2189420, 9 pages, 2017.

[28] L. G. Nallim, F. J. Bellomo, R. D. Quinteros, and S. Oller, "Dynamical analysis of long fiber-reinforced laminated plates with elastically restrained edges," *Advances in Acoustics and Vibration*, vol. 2012, 16 pages, 2012.

[29] A. K. N. Hafizah, J. H. Lee, Z. A. Aziz, and K. K. Viswanathan, "Vibration of antisymmetric angle-ply laminated plates of higher-order theory with variable thickness," *Mathematical Problems in Engineering*, vol. 2018, Article ID 7323628, 14 pages, 2018.

[30] G. Liu, W. Zhang, and A. Xi, "Nonlinear vibrations of laminated cross-ply composite cantilever plate in subsonic air flow," *Mathematical Problems in Engineering*, vol. 2020, Article ID 4601672, 19 pages, 2020.

[31] M. Baigang, Z. Hao, and Z. Jun, "Calculation of dynamic derivatives for aircraft based on CFD technique," *Acta Aerodynamica Sinica*, vol. 32, no. 6, pp. 834–839, 2014.

[32] H. Cho, J. Y. Kwak, S. J. Shin, N. Lee, and S. Lee, "Computational analysis for flapping wing by coupling the geometrically exact beam and preconditioned Navier-Stokes solution," in *55th AIAA/ASME/ASCE/AHS/ASC Structures, Structural Dynamics, and Materials Conference*, pp. 1–15, National Harbor, Maryland, 2014.

[33] Q. Zhou, D. F. Li, G. Chen, and Y. M. Li, "General static aeroelasticity analysis method based on CFD/CSM coupling," *Journal of Aerospace Power*, vol. 33, no. 2, pp. 355–363, 2018.

[34] T. Q. Guo, Z. L. Lu, and D. Zhou, *Aero-elastic CFD/CSD Coupling Calculation of Aircraft*, Science Press, Beijing, 2018.

[35] Q. Zhang, X. P. Zhu, Z. Zhou, and W. Wang, "Numerical research on static aeroelasticity of joined wing based on CFD/CSD coupling," *Journal of Northwestern Polytechnical University*, vol. 34, no. 3, pp. 347–442, 2016.

[36] C. Michele, E. Jonathan, and L. Yves, "Nonlinear static aeroelasticity of high-aspect-ratio-wing aircraft by finite element and multibody methods," *Journal of Aircraft*, vol. 54, no. 2, pp. 548–559, 2017.

[37] K. Ahmad, H. Rahman, and H. Hasham, "Nonlinear static aeroelastic analysis of high aspect ratio wing," in *Proceedings of 2014 11th International Bhurban Conference on Applied Sciences & Technology (IBCAST)*, pp. 349–353, Islamabad, Pakista, 2014.

[38] S. Lei, J. L. Wang, T. L. Li, W. S. Zhang, Z. G. Ren, and H. Cui, "Effect of material properties on nonlinear static aeroelastic properties of high- aspect- ratio wings," *Journal of Mechanical & Electrical Engineering*, vol. 37, no. 12, pp. 1432–1438, 2020.

[39] S. Hao, T. Ma, W. Gan, and G. Li, "Static aeroelastic characteristics analysis of high-aspect-ratio wing for hydrogen-powered UAV," *Journal of Beijing University of Aeronautics and Astronautics*, vol. 43, no. 8, pp. 1670–1676, 2017.

[40] J. Ballmann, A. Dafnis, H. Korsch et al., "Experimental analysis of high Reynolds number aerostructural dynamics in ETW," in *46th AIAA Aerospace Sciences Meeting and Exhibit*, Nevada, 2008.

[41] X. Y. Zhou, "Study on flexural and torsional coupling characteristics of composite blade for large wind turbine," *North China Electric Power University*, pp. 23–27, 2016.

[42] Z. H. Shi-quan, L. I. Hai-yuan, C. H. Zhi-hua, and Z. H. Hui, "Investigations of characteristics of static aeroelasticity for elastic wing," *Engineering Mechanics*, vol. 34, no. S1, pp. 326–332, 2017.

[43] B. P. Perry, J. P. Florance, J. Heeg, P. Chwalowski, and C. D. Wieseman, "Preliminary computational analysis of the HIRENASD configuration in preparation for the aeroelastic prediction workshop," in *IFASD*, Hampton, 2011.

[44] S. Yoon and A. Jameson, "Lower-upper Symmetric-Gauss-Seidel method for the Euler and Navier-Stokes equations," *AIAA Journal*, vol. 26, no. 9, pp. 1025-1026, 1988.